Integrated Design and Analysis of a Low-Cost, Motor-Driven Airbrake System for a Sounding Rocket

Juan Alizo Ewald*, Nicholas Dagnino†, Parsa Novin‡, Austin Applestone§, and Brooklyn Schnupp¶
University of Georgia, Athens, GA, 30605

This paper presents the integrated design, analysis, manufacturing, and control validation of a low-cost, motor-driven airbrake system developed by the University of Georgia Rocketry Team for the 2026 International Rocket Engineering Competition (IREC). The subsystem targets precise apogee regulation to a 10,000 ft (3048 m) goal while meeting strict constraints on size (225 mm axial length), mass (3.2 kg), current draw (25 A), and cost ($400). The mechanism employs three symmetric, radially curved flaps actuated by a ball-screw and linkage system driven by a NEO 550 BLDC motor and 4:1 gearbox. Material selections (7075-T6 for arms/linkages, 6061-T6 for the CNC'd cuff, and G10 for ribs and bulkheads) were guided by strength, fatigue resistance, and manufacturability. A kinematic-force optimization model was developed to minimize current draw, and worst-case aerodynamic loading informed component sizing. Finite element analysis verified acceptable stresses and deflections, while CFD characterized drag-producing flow features at 80° deployment and Mach 0.7. System-level performance was evaluated in RocketPy with Monte Carlo simulations, where an explicit model predictive controller (EMPC) delivered the lowest RMSE in apogee error across 370,000 runs. The resulting design provides a robust, manufacturable airbrake system capable of repeatable deployment and precise apogee control within student-team resource limits.

I. Nomenclature

C_d	=	drag coefficient
C_p	=	center of pressure, m
C_g	=	center of gravity, m
v	=	velocity, m/s
CFD	=	computational fluid dynamics
FEA	=	finite element analysis
$DFMA$	=	design for manufacturing and assembly
$SRAD$	=	student research and development

II. Introduction

The University of Georgia AIAA chapter has participated in the International Rocket Engineering Competition (IREC) since 2024. Every year, the team designs and manufactures a high-powered sounding rocket and has achieved 19th and 10th place out of 180+ universities internationally. The category that it competes in allocates 30% of the points to reaching a target apogee as close to 10,000 ft (3048 m) as possible. Similarly, 50 bonus points are reserved for Student Research and Development (SRAD). With the purpose of aiding in the apogee goal and SRAD requirement, the team has developed an airbrake mechanism that can actively control the projected apogee of the rocket by increasing drag through an electromechanical integrated system. It consists of three flaps that can be controlled to be between parallel and perpendicular to the body tube and direction of motion. With undeployed airbrakes, the rocket is designed to surpass the target apogee (at 3505 m), allowing the team to control how much it needs to be decreased by actively increasing the

*Mechanical Engineering Student, University of Georgia, AIAA Number #1810353
†Mechanical Engineering Student, University of Georgia, AIAA Number #1931478
‡Electrical Engineering Student, University of Georgia, AIAA Number #1810339
§Mechanical Engineering Student, University of Georgia, AIAA Number #1924172
¶Mechanical Engineering Graduate Student, University of Georgia, AIAA Number #1601486

drag in flight. This effort required collaboration between the SRAD, Embedded, and Simulations subteams, ensuring mission reliability and significant results.

III. Mechanical Design

In order to control the maximum apogee of the rocket, the SRAD team was tasked with designing a mechanism that would outwardly extend plates to reduce the rocket's velocity and apogee. Furthermore, a set of requirements had to be fulfilled: the mechanism had to fit within the rocket body tube's inner diameter of 151.765 mm (or 6 in.) and an axial length of 225 mm (or 8.9 in.), weigh under 3.2 kg (or 7 lb), draw less than 25 A of current, and cost less than USD 400.

The mechanism employs three symmetric, radially curved flaps offset by 120°, each with an area of 3870.96 mm^2, that are actuated between 0° and 80° from the vertical plane. The flaps are recessed into the body tube when inactive, reducing unwanted drag. To optimize the strength-to-weight ratio, 7075-T6 aluminum was selected for the flap arms and linkages due to its high yield strength and fatigue resistance under aerodynamic torque during deployment.

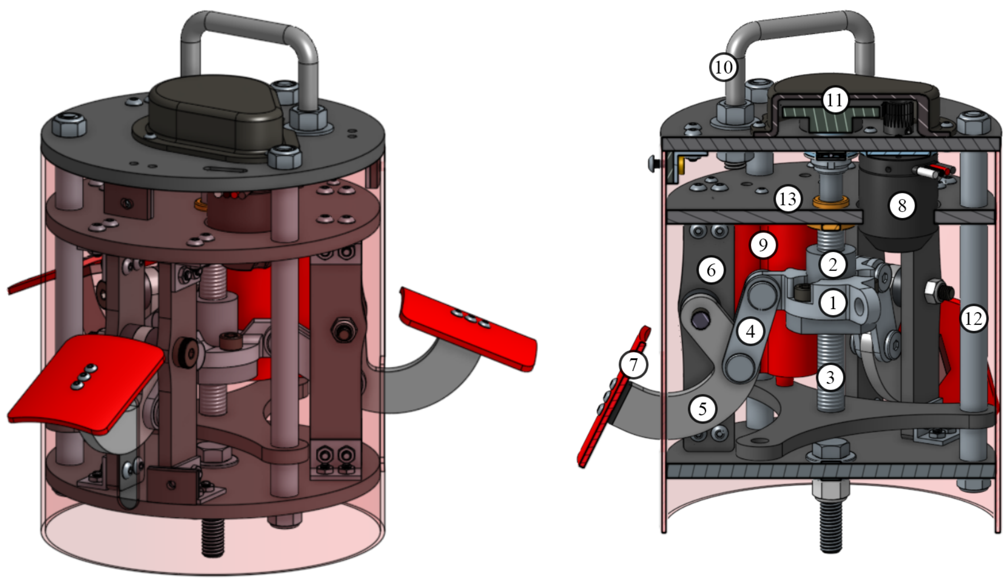

Fig. 1 Overview of the airbrake mechanism. Shown are the nut cuff (1), ballscrew nut (2), ballscrew (3), linkage (4), arm (5), rib (6), flap (7), motor (8), battery holder (9), U-bolt (10), gear and case (11), threaded rod and spacer (12), G10 plates (13).

The flaps are connected to a 7075-T6 aluminum arm that pivots about an M8 shoulder screw in the G10 vertical ribs. The arm connects via a 7075-T6 aluminum double-linkage to a custom CNC'ed 6061-T6 aluminum cuff mounted to the ball-screw nut, which slides axially on a 1204 ball screw. The 6061-T6 cuff was chosen for its machinability in complex CNC geometries while maintaining sufficient structural integrity.

The arm-to-cuff linkage pins are M8 stainless steel Chicago screws. The primary structural ribs are G10 fiberglass, selected for high compressive strength and precision waterjet cutting that holds a uniform tolerance of ±0.5 mm across the internal assembly. The ball screw is driven through a 4.0:1 gearbox by a NEO 550 BLDC motor. Through rotation of the motor, both clockwise and counterclockwise, the ball-screw nut translates vertically, deploying the flaps upward or downward accordingly.

The internal framework consists of forward and aft G10 plates held in compression by three M8 steel threaded rods and aluminum spacers, forming a rigid, lightweight cage that resists axial compression and vibration while providing mounting interfaces for the recovery system and motor casing. These spacers ensure structural integrity and accurate, repeatable positioning of the elements that constrain the ball-screw assembly.

The drogue parachute is attached to the top plate via a square 2.5 in. U-bolt, and the motor tube is attached to the bottom plate. Inside, two additional G10 plates constrain the ball screw. The standard 1204 ball screw is maintained in position by flanged sleeve bearings. These bearings withstand axial loads up to 3500 N (or 800 lb) and also act as thrust bearings. To constrain the forward section of the ball screw, an M10 x 1.0 mm bearing locknut, set screw, and C-clip secure the bearing stack at the bottom of the threaded section. A high-load thrust bearing rated for 9120 N (or 2050 lb) and a maximum speed of 17000 rpm rests on this bearing locknut. This bearing arrangement transfers aerodynamic loads through the 7075-T6 linkages into the structural bulkheads rather than the motor shaft, limiting elastic deformation of the arms and enabling consistent, repeatable deployment. The bottom of the first section of the ball screw rests within a flanged bearing that resists radial loads from the motor. Above this flanged bearing, a 96-tooth gear meshes with the 24-tooth motor-driven gear.

IV. Analysis and Optimization

To calculate the airbrake's impact on the target apogee, the drag at different actuation levels was analyzed. Similarly, to ensure the current draw stays within our margins (25 [A]), to enable the motor to provide sufficient torque, and to ensure the mechanical components have a factor of safety of over 1.25, the force on the flaps was calculated at the worst-case scenario. For the worst-case scenario, the airbrake system would be fully deployed (100° downward with respect to the fluid flow, nearing perpendicularity) at maximum speed (Mach 0.981, exactly after burnout). It should be noted that this scenario is highly unlikely.

A. Low Fidelity Analysis

To conduct initial sizing estimations, the team used OpenVSP AERO to obtain drag coefficients at different flap areas and flap angles (), modelled by angle of attack. The simulation was performed using a NACA 0012 airfoil to replicate a flap moving from an undeployed position to full actuation at values of 0 to 90 deg and an area of 1 in² to 8 in², at a step size of 1 in². Individual Cd values were paired with values and used to calculate the force acting on the flap at different actuation levels and flap sizes. The density and velocity values used in the drag force equation were based on a maximum Mach at burnout of 0.981 and flap actuation at 2,133 m, which takes into account the launch site elevation of 914 m and an altitude at burnout of 1219 m. The results were imported to the geometry optimization algorithm, which helped determine an adequate flap size based on factors such as control authority and maximum allowable force on the linkages.

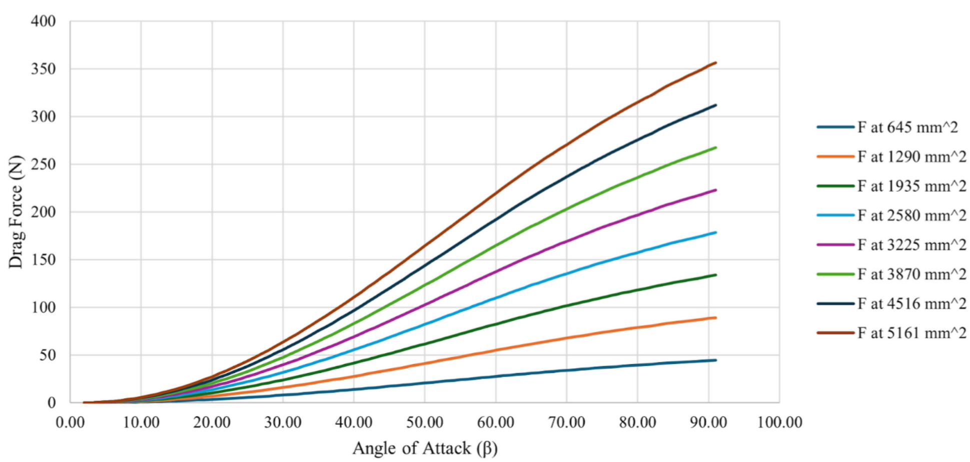

Fig. 2 Drag Force at various flap areas

B. Kinematic and Force Relations

One of the airbrake's requirements is to draw less than 25 A of current. This maximum was set to ensure that the battery capacity remains within functional and effective operating range throughout the entire flight time. The current draw is based on the torque, which in turn is based on the total axial force applied on the nut by the three flaps. Due to the linkage geometry, the axial force transferred to the ballscrew nut by the flaps is not linearly proportional with actuation. This is highly dependent on the position of the pins, as well as the length of the moment arms/linkages. The original goal was to simply calculate the current draw on the first airbrake iteration, which had a largely arbitrary linkage geometry. As a kinematic model was built, it became apparent that the geometry could be optimized following the same mathematical/engineering concepts. Consequently, the team developed a kinematic-force model that iterates through different geometry combinations to minimize the current draw while taking into account space constraints.

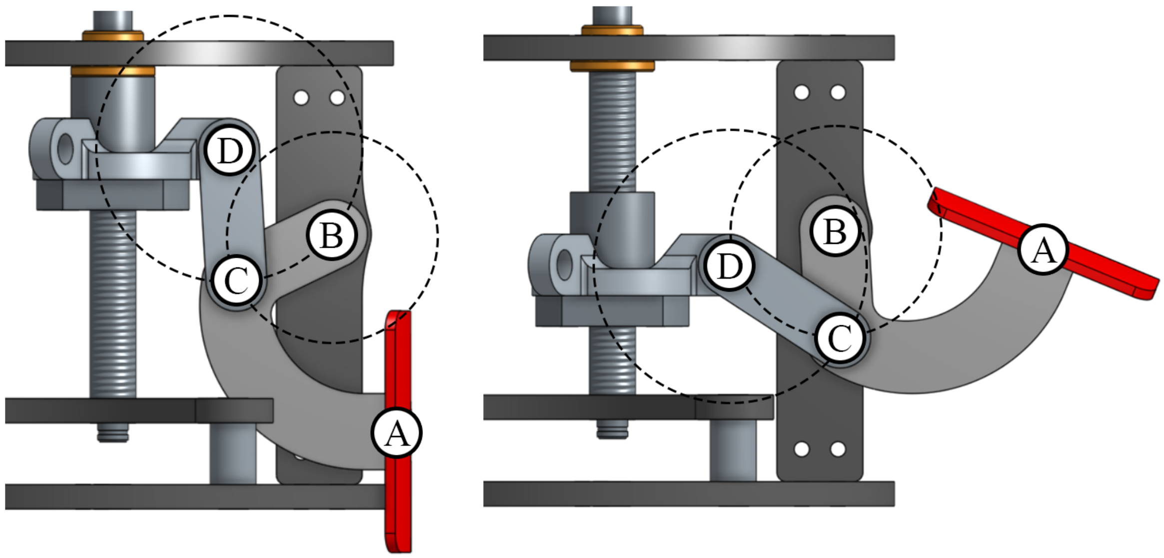

Fig. 3 Linkage geometry used in the kinematic-force model, shown at two actuation states. Shown are the flap connection point (A), pivot pin (B), linkage-pivot connection (C), and cuff-linkage pin (D).

The actuation of the flaps can be described as a function of the displacement of the nut, but some relations need to be defined before that. The linkage and pivot arm can be imagined as two circles. The center of Circle D is the position of the cuff-linkage pin (D_x, D_y), and its radius $(\overline{DC})$ is the linkage length. The center of Circle B is the position of the pivot pin in the pivot arm (B_x, B_y), and its radius $(\overline{BC})$ is the distance between the linkage pin and the pivot point:

$$(x - D_x)^2 + (y - D_y)^2 = (\overline{DC})^2 \tag{1}$$

$$(x - B_x)^2 + (y - B_y)^2 = (\overline{BC})^2 \tag{2}$$

Now that these two circles are set, the position of the last pin (C_x, C_y) can be defined. This pin is the point connecting the linkage and the pivot arm, and can be represented as the lower intersection point between the two circles. To calculate it, the distance between CD and CB (d), distance from CB to the midpoint of the intersection points (a), and height connecting CD and CB to the intersection points (h) are needed:

$$d = \sqrt{(D_x - B_x)^2 + (D_y - B_y)^2} \tag{3}$$

$$a = \frac{(\overline{DC})^2 - (\overline{BC})^2 + d^2}{2d} \tag{4}$$

$$h = \sqrt{(\overline{DC})^2 - a^2} \tag{5}$$

Similarly, the point where the two intersection points and the two centers intersect can be calculated (x_0, y_0):

$$x_0 = D_x + a\frac{(B_x - D_x)}{d} \tag{6}$$

$$y_0 = D_y + a\frac{(B_y - D_y)}{d} \tag{7}$$

Finally, the coordinates for the position of the third pin (connecting linkage to pivot arm) is defined by:

$$C_x = x_0 + h\frac{(B_y - D_y)}{d} \tag{8}$$

$$C_y = y_0 - h\frac{(B_x - D_x)}{d} \tag{9}$$

This showcases the mathematical relation between the different points. That said, in the algorithm used for the optimization, a slightly different approach is taken. Instead of setting the position and radii of both circles (for points B and D), the position of three points (B, C, and D) is inputted, with the distance between them being calculated later. This decision was made because it facilitates the usage of allowable ranges for point C, making it easier to apply geometric constraints.

$$C_x = D_x + a\frac{(B_x - D_x)}{\overline{BD}} + h\frac{(B_y - D_y)}{\overline{BD}} \tag{10}$$

$$C_y = D_y + a\frac{(B_y - D_y)}{\overline{BD}} - h\frac{(B_x - D_x)}{\overline{BD}} \tag{11}$$

Now the internal relations have all been defined. By moving Circle D along the y-axis (altering D_y), it can be seen how the linkage and pivot arm would move as the nut linkage travels along the ball screw. When given initial conditions, this enables the tracking of a point along the entire range of actuation. The change in the y-coordinate for D is represented by ΔD_y, and each motor revolution equates to equates to a ΔD_y of 1mm:

$$D_y = D_{y,0} - \Delta D_y \tag{12}$$

The cuff pin (D) can move vertically (D_y) but not horizontally (D_x), the pivot pin (B) is fixed in both directions (B_x, B_y), and the linkage-arm pin (C) can move in both directions (C_x, C_y). To perform the force calculations, some angles of interest are needed.

The angle between the horizontal plane and the linkage is:

$$\theta = -\arctan\left(\frac{D_y - C_y}{D_x - C_x}\right) \tag{13}$$

The angle between the vertical plane and the pivot-linkage is:

$$\phi = \arctan\left(\frac{B_x - C_x}{B_y - C_y}\right) \tag{14}$$

The actuation angle is defined between the flap and the body tube; it is referred to as β.

$$\beta = \phi - \phi_0 \tag{15}$$

Similarly, the position of the plate is defined by the actuation. Since its local position within the arm is fixed, it moves in a circular motion around the pivot. The global coordinates of the flap's connection point (A) can be defined as:

$$A_x(\beta) = B_x + (A_{x,0} - B_x)\cos\beta - (A_{y,0} - B_y)\sin\beta \tag{16}$$

$$A_y(\beta) = B_y + (A_{x,0} - B_x)\sin\beta + (A_{y,0} - B_y)\cos\beta \tag{17}$$

The last thing needed is the force acting on the plates. After simulating the drag at different actuation levels, a trendline (with an $R^2 = 0.999$) was calculated:

$$F_A(\beta) = -0.0005\beta^3 + 0.0861\beta^2 - 0.5486\beta + 1.2015 \tag{18}$$

Knowing the force on the flaps as a function of β, the equation for the total force acting on the nut from one flap as a function of the nut's displacement is the following. Note that this specific equation uses the coordinate origin at point B.

$$F = \frac{F_a(sin(\beta)A_y + cos(\beta)A_x)}{C_x\sin(\theta) - C_y\cos(\theta)} \tag{19}$$

The total axial force acting on the nut from all three plates is:

$$F_{\text{axial}} = (3)(F)\sin(\theta) \tag{20}$$

To calculate the torque, gear ratio (G), lead (l), and efficiency (η) of the ballscrew are needed.

$$T = \frac{F_{\text{axial}}\,l}{2\pi\eta\,G} \tag{21}$$

Finally, the current draw is characterized by:

$$I_{\text{draw}} = I_{\text{free}} + \left(\frac{I_{\text{stall}} - I_{\text{free}}}{T_{\text{stall}}}\right)T \tag{22}$$

C. Geometry Optimization Algorithm

Utilizing the previous kinematic and force relations, the team developed a python algorithm that iterates through a combination of pin positions to find the most optimal. Each pin is given a coordinate range it can physically exist within (at the starting point) as well as a set of constraints the system needs to abide by.

1) Create the search range: Iterate through all discrete combinations of defined coordinates for the pivot (B), the flap (A), the linkage pin (C), and the initial nut pin position (D).

2) Calculate Rigid Geometry: For each coordinate combination, calculate the permanent arm lengths and the fixed internal angle offset of the airbrake plate. Refer to Eqs. (1) and (2).

3) Simulate the Stroke: Actuate the ball nut (D) downwards in discrete vertical steps across the predefined stroke length. Refer to Eq. (12).

4) Resolve Kinematics: At each step, calculate the new global coordinates of C using circle-circle intersection, and update the position of A via rigid body rotation. Refer to Eqs. (10), (11), (16), and (17).

5) Enforce Geometric Constraints: Immediately discard the configuration if the circles fail to intersect (indicating mechanism lockup/binding) or if C enters the defined keep-out zone (interfering with airframe ribs).

6) Calculate Quasi-Static Forces: At each step, evaluate the forces in the system using the CFD polynomial, and resolve the resulting axial and radial (side) loads on the nut. Refer to Eqs. (18), (19), and (20).

7) Apply Mechanical Limits: Discard the configuration if the instantaneous radial side load on the nut cuff exceeds the maximum allowable threshold at any point during the stroke.

8) Verify Deployment Angle: After completing the stroke simulation, confirm that the final swing angle of the airbrake falls within the targeted operational range (in our case, 79° to 81°).

9) Optimize: If the configuration fulfills all kinematic, geometric, and mechanical constraints, compare its peak axial load to the current recorded minimum. If it requires less axial force, record it as the new optimal design. Then, calculate current draw using Eqs. (21) and (22).

The algorithm was initially run with the low-fidelity drag force magnitudes to determine rough sizing. The flap area was decided to be 3870.96 mm^2, as it provided the most drag while still within the allowable current draw range. At first, over 1,500,000 point combinations were evaluated, and the range was slowly reduced and resolution increased. Assuming that the airbrakes deploy in this worst-case scenario (Mach 0.981), the maximum current draw would be 17 A, and it would occur when the flap angle (β) is at 60°.

D. Finite Element Analysis

To ensure the structural integrity of the system, static-structural FEA analysis was performed on a simplified model of the mechanism. Since it is a dynamic component, it was simulated at different discrete actuation levels. The force exerted on the flap is 256 N and acts perpendicular to its face. This number is extracted from the maximum force that the flap would experience in the worst-case scenario immediately after burnout (refer to Eq.18). Von Misses stress was utilized due to the ductile nature of the components of interest.

The results validated points that were previously identified as possible critical failure areas. Pin C witnesses the largest equivalent stress at 95 MPa, and with a standard stainless steel's yield strength of 215 MPa results in a FS of 2.26. It is worth emphasizing that the pins are chicago screws, and the manufacturer does not provide the precise material properties. This increases the uncertainty in the results, but it is compensated by the large factor of safety.

The deformation in the z-direction (vertical) also follows expected patterns. Although it may look as if there is little deformation in the tip of the arm and a lot in the rib/linkage, it must be noted that the maximum refers to largest in the positive Z direction, not the absolute magnitude. The maximum deformation magnitude does indeed occur at the tip of the arm, with 0.14 mm of downward deformation, and is negligible on the other points of interest.

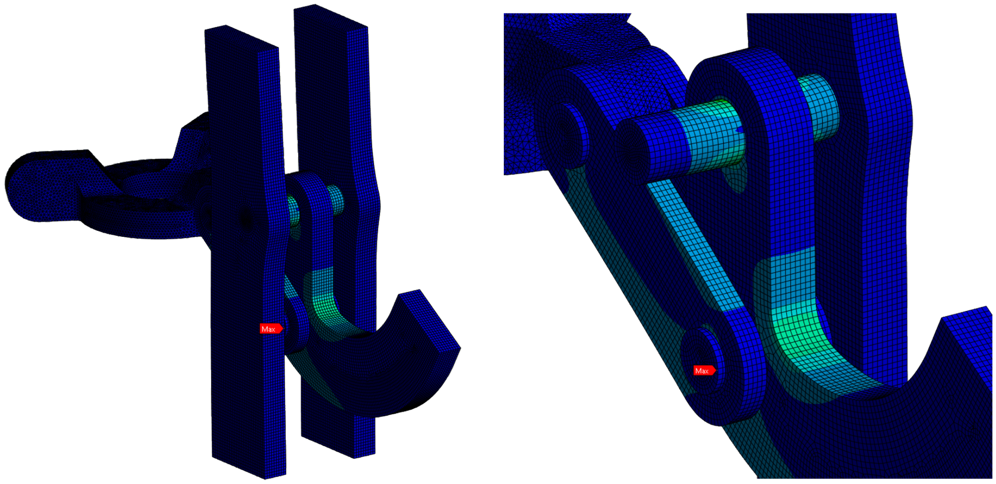

Fig. 4 Equivalent stresses from static structural analysis.

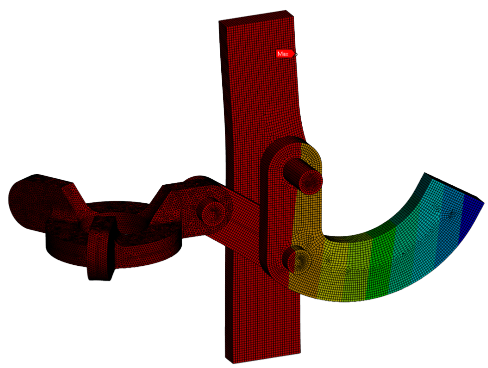

Fig. 5 Deformation in Z direction.

E. Computational Fluid Dynamics

Computational Fluid Dynamics (CFD) analysis was performed using Ansys Fluent to validate the structural loading and control authority of the airbrake system. The simulation focused on a maximum deployment angle of 80° at a velocity of Mach 0.7 to replicate flight-like conditions where the airbrakes encounter high aerodynamic loading. The flow field shows local acceleration around the flap tips, elevated static pressure on the windward face of the flaps, and total-pressure loss in the wake, which together confirm the expected drag-producing behavior and support the loading assumptions used in the structural and control analyses. This number differs from the low fidelity analaysis, primarily due to the difference in velocity used. CFD simulations were run using Mach 0.7 and OpenVSP used worst case scenario at max velocity of Mach .981.

For modeling simplicity, the airbrakes were simulated without the physical gap between the flap and the airframe. This geometric simplification increases the total effective surface area, resulting in a conservative overestimation of the total drag force and the coefficient of drag (C_d). By deliberately overestimating these real-world forces, the team ensured that the structural design remains within safe operating limits even under conditions exceeding expected flight loads. The results indicate that pressure drag is the dominant force in this regime. Outside of the flap edges, the pressure distribution remains relatively uniform, with the resultant distributed load located at the centroid of each plate. The

Fig. 6 Mach number contours at 80° deployment and Mach 0.7, showing local acceleration near flap edges.

Fig. 7 Static pressure contours at 80° deployment and Mach 0.7, showing elevated pressure on the windward face.

Fig. 8 Total pressure contours at 80° deployment and Mach 0.7, showing wake losses behind the flaps.

simulation yielded a total force of 320 N across all three flaps (106 N per flap), confirming that the mechanism possesses the necessary authority to meet performance requirements while remaining structurally sound.

V. Control System Design

The basis of the airbrake system's electrical control is the link between the NEO 550's bi-directional Electronic Speed Controller (ESC) and the avionics bay's STM32H5 microcontroller, responsible for running the control loop to calculate required plant state (the actuation level of the airbrakes flaps). In order to keep avionics centralized due to cost limitations, the STM modulates the speed of the BLDC via the ESC through a 2-wire magnetic link to the airbrakes bay from the avionics bay by PWM, ranging from 10 to 20ms in pulse length with 15ms as the stop point, where opposing lobes in the range have opposite directions for running the BLDC. Feedback from the motor's position is updated through the NEO 550's 3-phase hall encoder at 42 counts per revolution, also fed through the airbrakes bay into the avionics bay. The ball screw's change in elevation relates to 1mm per rotation of the NEO 550 (refer to Eq. 12), and therefore the position of the ball screw is able to be determined throughout the control loop. In all pre-flight checklists, a manual absolute position reset is required at the beginning of each flight (achieved through an Electrical Ground Support Equipment (EGSE) umbilical link to the team's embedded Human-Machine-Interface (HMI)). To determine

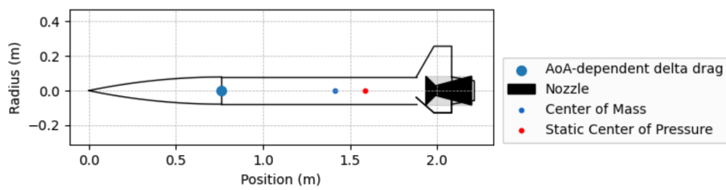

Fig. 9 Simplified rocket representation.

the controller of the airbrakes' feedback control system, virtual software-in-the-loop (SIL) testing was completed in a partially custom-built flight simulator using the RocketPy library. The environment and rocket models were built using historical weather data and all approximations of the final manufactured rocket including .eng data of the M3400 CTI motor, and Computer-Aided-Design (CAD) data of material-assigned models for center of gravity and inertia tensor matrices. The open source software OpenRocket was used as a comparison tool to determine initial simulation fidelity, with nominal data sets shown in the figures below.

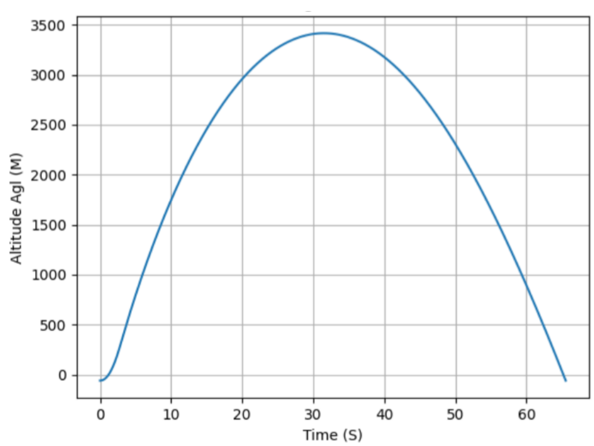

Fig. 10 Altitude above ground level vs. time.

Coefficient of drag data provided by CFD simulations through Mach and angle of attack sweeps, in addition to the IREC launch environment data, were used to adjust possible launch parameters in Monte Carlo simulations. The plant of the feedback system was approximated using a GenericSurface object inside the RocketPy library, allowing for simulation index instantaneous modulation of the coefficient of drag as a function of the controller's normalized output, u. The average error and Root Mean Square Error (RSME) of the following controllers were approximated across 370,000 simulations per controller:

Across the completed simulations, the mean apogee error Y indicates the bias of the controllers against the 3048 reference point, and RSME indicates the absolute value of the average error in apogee. The EMPC's calculated RSME placed it as the most consistent controller with a small amount of scatter in its runs. The PID controller has a relatively

Table 2 Controller error statistics from Monte Carlo simulations.

Controller	ΔY (m)	RSME (m)
Proportional Integral Derivative (PID)	-33.41	127.70
Explicit Model Predictive Controller (EMPC)	-9.19	19.03
Linear Quadratic Regulator (LQR)	40.03	44.95
Cascade Control	-49.02	76.11

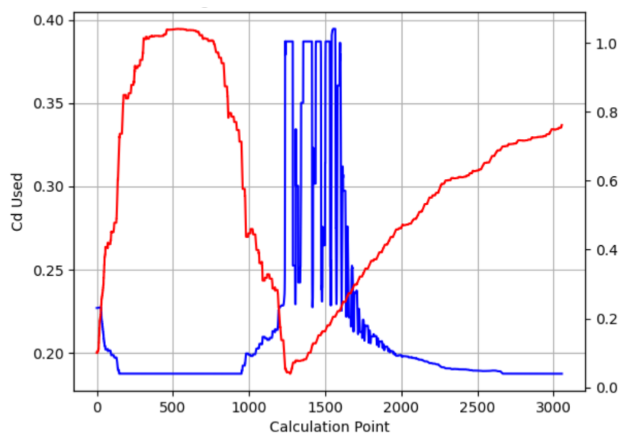

Fig. 11 Mach and drag coefficients values at calculation indices.

low mean error but a comparatively much larger RSME, indicating a larger amount of range in the PID's performance, nonoptimal for the addition of noise in implementation. The LQR and Cascade Controllers are similar in results, with the LQR being noticeably better in its RSME.

Characterization of the physical airbrake system will be completed along with updates to the plant. For further development and testing with hardware integration and Hardware-in-the-Loop Testing (HIL), the EMPC will be adapted to C code running on the STM32H5 in the avionics bay Printed Circuit Board (PCB) stackup. Controller design will be re-evaluated with physical realization of the simulations and plant limitations.

VI. Manufacturing and Integration

The manufacturing phase prioritized Design for Manufacturing and Assembly (DFMA) to mitigate the financial and schedule risks inherent in custom aerospace fabrication. To optimize resource allocation, the production strategy adhered to three primary constraints: (1) maximizing the utilization of existing material stock, (2) standardizing hardware through the use of Commercial Off-The-Shelf (COTS) fasteners, and (3) minimizing custom-machined parts to only those that exemplify difficulties regarding manufacturing. Following the Critical Design Review (CDR), all standardized components were procured, while in-house fabrication focused on G10 fiberglass elements processed via waterjet cutting to ensure a uniform tolerance of ±0.5 mm. Additional 3D printed, non-structural components were produced using resources available to the team. For components requiring higher structural density or complex geometries, specifically the sheet metal flap arms, linkages, and the ball screw nut cuff, external machining and waterjetting was utilized to maintain the project timeline without compromising component precision.

Integration represents the most critical assembly phase, as the physical hardware must be reconciled with the nominal computerized model to account for real-world variances. The system is designed for modularity; the primary airbrake assembly, with control flaps removed, is loaded into the body tube in a single operation. Proper radial and axial alignment is facilitated by precision cutouts in the airframe and internal supporting coupler. Three M4 screws, distributed symmetrically above the flap bays, secure the internal module and ensure the deployment linkages remain centered. Once the internal structure is fixed, the flaps are attached to the rotating arms using three M3 screws per flap, allowing them to sit flush within the recessed sections of the body tube. Finally, the solid rocket motor casing is loaded through the aft end of the rocket. The casing is threaded onto a 3/8-16 fastener mounted at the base of the airbrake assembly and rotated until fully torqued. This connection serves as the primary structural interface between the propulsion system and the airbrake module, completing the integration sequence in preparation for testing and flight operations.

VII. Conclusion

This research demonstrated the integrated design, analysis, manufacturing, and control validation of a low-cost, motor-driven airbrake system developed by the University of Georgia Rocketry Team for the 2026 International Rocket Engineering Competition. The system was designed to satisfy strict geometric, mass, electrical, and financial constraints while providing sufficient control authority to modulate a nominal 3,505 m trajectory down to the 3,048 m (10,000 ft) target apogee in real time. A mechanically robust and manufacturable architecture was achieved through a three-flap, ball screw–actuated linkage system powered by a NEO 550 BLDC motor and 4:1 gearbox. Analytical drag modeling, kinematic-force optimization, and worst-case loading scenarios informed the final geometry size, ensuring current draw remained below 25 A and structural components maintained acceptable safety margins. CFD and low-fidelity aerodynamic modeling provided drag characterization across actuation angles, supplying accurate force inputs to both structural and control simulations. FEA verified that peak stresses, particularly at critical linkage pins, remained well below material yield strengths, with conservative factors of safety compensating for uncertainty in manufacturer-specified hardware properties.

Control system development further demonstrated the feasibility of precise apogee regulation. Through extensive Software-in-the-Loop simulations in RocketPy, including over 370,000 Monte Carlo runs per controller architecture, the Explicit Model Predictive Controller (EMPC) emerged as the most consistent strategy, achieving the lowest root mean square apogee error. These results indicate strong robustness to environmental variability and modeling uncertainty, positioning the EMPC as the primary candidate for hardware implementation and Hardware-in-the-Loop validation. Equally important, the design emphasizes rapid manufacturability and integration using in-house fabrication capabilities and commercial off-the-shelf components. The modular assembly approach simplifies installation within the airframe and reduces alignment sensitivity, addressing practical challenges observed in previous iterations.

Overall, the resulting airbrake system represents a balanced solution that integrates aerodynamics, structural mechanics, controls, and manufacturing within a constrained student-team environment. The validated analyses and simulation results demonstrate that the system is capable of withstanding expected flight loads while delivering reliable, high-precision apogee control. Future work will focus on full-system characterization, hardware-in-the-loop testing, and iterative controller refinement to further reduce apogee dispersion and enhance flight reliability at IREC 2026.

References

[1] "RocketPy Documentation — RocketPy 1.11.0 documentation," Retrieved from https://docs.rocketpy.org/en/1.11.0/, n.d. Online documentation.

[2] REV Robotics, "REV-21-1651 Product Page," Retrieved from https://www.revrobotics.com/rev-21-1651/, n.d. Product page.

[3] Budynas, R. G., and Nisbett, J. K., *Shigley's Mechanical Engineering Design*, 10^{th} ed., McGraw-Hill, New York, NY, 20XX.

[4] Aaron, R. F., "Altitude-Limiting Airbrake System for Small-Medium Scale Rockets," Tech. Rep. NASA USRP-Internship Final Report KSC-E-DAA-TN12413/KSC-2013-313, NASA, Kennedy Space Center, FL, Dec. 2013. URL `https://ntrs.nasa.gov/api/citations/20140013095/downloads/20140013095.pdf`.

[5] Barrowman, J. S., "The Practical Calculation of the Aerodynamic Characteristics of Slender Finned Vehicles," Tech. Rep. NASA-TN-D-6248, NASA, 1967. URL `https://ntrs.nasa.gov/citations/20010047838`.

[6] Anderson, J. D., *Fundamentals of Aerodynamics*, 6^{th} ed., McGraw-Hill Education, New York, NY, USA, 2016.

[7] Chaudhard, B., "CFD-Based Aerodynamic Modeling and Validation of Airbrake Integration for Apogee Control in a Sounding Rocket," Tech. rep., UGA Rocketry, 2026.